Ultrathin Ni-Mo oxide nanoflakes for high-performance supercapacitor electrodes

Harish. S. Chavan,[†] Bo Hou,[‡] Abu Talha Aqueel Ahned,[†] Jongmin Kim,[†] Yongcheol Jo,[†] Sangeun Cho,[†] Sambhaji M. Pawar, [†] Akbar I. Inamdar,[,†] Jayavant L. Gunjakar,[†] SeungNam Cha,[‡] Hyunsik Im[*,†] and Hyungsang Kim[*,†]*

† Division of Physics and Semiconductor Science, Dongguk University, Seoul 04620, South Korea

‡ Department of Engineering Science, University of Oxford, Parks Road, OX1 3PJ, UK

ABSTRACT: Supercapacitors based on nanomaterial electrodes exhibit great potential as power sources for advanced electronic devices. From a practical viewpoint, it is desirable to fabricate highly active and sustainable nanomaterial electrodes consisting of non-precious elements using a simple technique in a controllable way. In this work, we report the synthesis of a self-assembled ultra-thin porous nanoflake Ni-Mo oxide (NMO) film using the successive ionic layer adsorption and reaction (SILAR) technique. The nanoflake NMO thin film electrode with a large electrochemically active surface area of ∼108 cm−2 exhibits a high specific capacitance of 1180 Fg−1 at a current density of 1 Ag−1 and excellent rate capability, with a negligible capacity loss of 0.075% per cycle. Even at a high current rate of 10 A g−1 it retains a capacity of 600 Fg−1. The highest energy and power densities obtained are 119 Whkg−1 and 15.7 kWkg−1, respectively. Electrochemical impedance spectroscopy analyses reveal that the electrode has considerably low charge transfer resistance. The observed excellent electrochemical energy storage performance of the nanoflake NMO electrode with a nanoporous surface is due to the synergetic effects of the large electrochemically active surface area, enhanced ion diffusion, and improved electrical conductivity.

KEYWORDS: *Supercapacitor, Ni-Mo oxide nanoflake, Electrochemical active surface area, Successive ionic layer adsorption and reaction*

Corresponding authors

*Email: hskim@dongguk.edu, hyunsik7@dongguk.edu, akbarphysics2002@gmail.com

1. Introduction

The development of clean and environmentally-friendly energy sources is a key to fundamentally solve environmental pollution caused by human activities [1-6]. An outstanding example of clean energy storage devices is the supercapacitor, which has become a core component in various technologies, such as portable electronic devices, electric hybrid vehicles, and medical equipment. A crucial factor for the commercialization of supercapacitors is the development of environmentally-friendly electrodes that can be fabricated at low cost, provide high energy/power densities and have excellent stability. Carbon materials, polymer-based materials, and transition metal oxides have been widely studied for their application as supercapacitor electrodes. Carbon materials have small specific capacities, and polymer based materials have demonstrated insufficient electrochemical stability [7]. Transition metal oxides are promising electrode materials because of their high-capacity, long-cycle-life performance and environmental friendliness [8-15].

Binary metal oxides ($M1_xM2_yO_z$, where M1 and M2 represent different transition metals) have attracted attention for electrochemical energy storage because of the possibility to optimally engineer multiple oxidation states and electrical conductivity, which have not been achieved with single metal oxides and carbon-based materials [1, 5, 16-22]. The increased charge storage of this material is due to the synergetic effect of increased conductivity due to the metal element and high electrochemical activity of the other metal ions [23-25]. Various types of morphologies are grown to improve electrochemical performance, such as nanorods, nanowires, honeycomb, nanosheets, porous network, nanospheres. The detailed information about the morphologies and their electrochemical performance is presented in Table 1 [1, 4, 6, 7, 26-34]. Our review of the literature found that $NiMoO_4$ thin film deposition by the successive ionic layer adsorption and reaction (SILAR) technique has not yet been achieved.

This paper reports for the first time the synthesis of $NiMoO_4$ compound thin films

using a successive ionic layer adsorption and reaction (SILAR) technique for electrochemical asymmetric supercapacitor applications. The constituting Ni and Mo elements produce the synergetic effect of a large electrochemical active surface area, enhanced diffusion ions, lower charge transfer resistance and high electrochemical activity. We demonstrate excellent electrochemical supercapacitor electrode performance of the $NiMoO_4$ compound film.

2. Experimental Details

2.1 Synthesis of $NiMoO_4$ thin films

$NiMoO_4$ compound thin films were fabricated on stainless steel substrates using an SILAR technique. The precursor solutions were prepared using 0.1M $NiCl_2{\cdot}6H_2O$ and 0.1M $NaMoO_4{\cdot}2H_2O$. The pH of the Ni-containing bath was adjusted to 12.2 by adding an ammonia solution dropwise. The Mo-containing bath was maintained at 65 ^{0}C. The $NiMoO_4$ film was fabricated by successively dipping a stainless-steel substrate in each bath. One cycle consisted of 20 s dipping in the Ni-containing bath, 10 s in D. I. water, 20 s in the Mo-containing bath, and again 10 s in D.I. water. During each cycle, ion adsorption and nucleation processes occurred on the substrate, leading to the formation of a $NiMoO_4$ compound film. The $NiMoO_4$ thin film was grown at 35 successive cycles. The schematic diagram of the SILAR technique for the synthesis of $NiMoO_4$ is presented in supporting information Fig.S1. The film was dried at 100^0 C for 2 hrs to remove the water content and to increase their adhesion to the substrate.

2.2 Electrochemical Measurements

The electrochemical supercapacitor performance of the NiMoO4 electrode was investigated using cyclic voltammetry (CV), galvanostatic charge/discharge, and AC impendence analysis. A potentiostat (Princeton Applied Research, Versa STAT 3) was used with a conventional three-electrode electrochemical cell containing 2 M KOH as an electrolyte,

NiMoO4 as a working electrode, a saturated calomel electrode (SCE) as the reference electrode, and graphite as the counter-electrode. Electrochemical impedance spectroscopy (EIS) measurements were performed in an AC frequency ranging from 0.2 Hz to 10 kHz using an impedance analyzer. X-ray diffraction (XRD) patterns of the films were recorded using an X-ray diffractometer with Ni-filtered Cu-Kα radiation (Kα-1.54056 Å, X-pert PRO, Panalytical). Surface morphology was observed by using field emission scanning electron microscopy (FE-SEM, model: JSM-6701F, JEOL, Japan), and the chemical states of the NiMoO4 film were investigated using X-ray photoelectron spectroscopy (XPS, Ulvac -phi, Verse probe II). The microscopic properties of the sample were studied using scanning transmission electron microscopy (STEM, JEOL 2010 with an Oxford EDS detector) and high-resolution transmission electron microscopy (HRTEM, JEOL JEM-3000F FEGTEM), and selected area electron diffraction (SAED, 300kV).

3. Results and Discussion

Figure 1(a) shows the XRD pattern of the $NiMoO_4$ thin film with the standard JCPDS card (NO-45-0142) for $NiMoO_4$. The X-ray diffraction peaks at 2θ angles of 23.2, 34.9, 64.6, and 82.0 correspond to the crystallographic planes of (0 2 -1), (2 2 -2), (3 3 3), and (2 0 -6), respectively. A star symbol indicates the X-ray diffraction peaks of the substrate. The formation of $NiMoO_4$ was further confirmed by μ-Raman spectroscopy analysis. Figure 1(b) shows the μ-Raman spectrum of the $NiMoO_4$ thin film. Three vibrational bands are detected at 315, 854, and 909 cm^{-1}, which are typical of $[MoO_4]^{-2}$. The vibrational band at 909 cm^{-1} is associated with symmetric stretching modes of Mo-O-Mo vibrations, whereas the band at 854 cm^{-1} is related to asymmetric stretching modes. The vibrational band at 315 cm^{-1} is linked with symmetric bending modes of vibrations [23, 35, 36]. The broadness of the peaks is presumably a consequence of the nanocrystalline nature of the $NiMoO_4$. Figure 1(c) shows the FE-SEM

image of the $NiMoO_4$ thin film. The film shows a porous sponge-like morphology consisting of nanoflake networks. The thickness of $NiMoO_4$ nanoflakes is less than 10 nm.

The microstructure of the $NiMoO_4$ film is examined using HRTEM, SAED and high angle annular dark field (HAADF) STEM image as shown in Fig. 2 (a-g). The local HRTEM images (Figs. 2(a-b)) reveal the crystallized nature of as-prepared films. The observed lattice spacing from the lattice fringes in the HRTEM image is 0.21 nm, which corresponds to the {222) plane of $NiMoO_4$ (JCPDS-45-0142). The indexed SAED pattern further revealed the $NiMoO_4$ Monoclinic crystal structure (Fig. 2(c)) and the diffused rings observed in the SEAD pattern confirms the polycrystalline nature of the sample. Figures 2 (d- g) show the HAADF STEM and element mapping images of the sample (line scans provided in the supporting information Fig.S2), which demonstrate the homogeneous distribution of Ni, Mo and O. The EDS line profile (Fig. S2) carried out within 1μm dimension which further confirms the presence of Ni, Mo and O and the estimated element ratio of Ni and Mo was 51.72 and 48.28%, respectively (oxygen excluded).

XPS analysis was carried out to determine the chemical binding states of the $NiMoO_4$ thin film. Figure 3 (a) shows the wide-scan survey XPS spectrum of the $NiMoO_4$ thin film, confirming the presence of nickel (Ni), molybdenum (Mo), oxygen (O) which is consistent with our electron microscopy analysis. Figures 3 (b), (c), and (d) show the Ni*2p*, Mo*3d* and O*1s* core level spectra of the sample. The deconvoluted Ni*2p* spectrum shows two sets of peaks (main and satellite peaks), which correspond to Ni$2p_{3/2}$ and Ni$2p_{1/2}$, respectively, indicating the presence of Ni^{2+} [7, 23, 37]. The Mo*3d* spectrum shows two peaks at 231.12 eV and 234.25 eV, which associate to Mo$3d_{5/2}$ and Mo$3d_{3/2,}$ respectively [23, 38]. The binding energy difference between these two peaks is about 3.13 eV, which indicates the presence of Mo^{6+} in the film. The peak appearing at 530.5 eV in the O*1s* spectrum corresponds to metal-oxide bonds [23, 33]. The XPS results reveal that the $NiMoO_4$ sample contains Ni^{2+} and Mo^{6+} oxidation

states.

We investigated the electrochemical properties of the $NiMoO_4$ thin film using cyclic voltammetry (CV) and galvanostatic charge-discharge measurements. Figure 4 (a) shows the CV curves of the sample at various scan rates. The shape of the observed CV curves is different from the ideal rectangular shape, indicating the pseudocapacitive behavior of the electrode. Peaks observed at 0.22 and 0.35 V (vs. SCE) are respectively due to the reversible reduction and oxidation of the $NiMoO_4$ electrode. The area under the CV curve is directly proportional to the specific capacity of the electrode, and the similar shape of the CV curves at different scan rates suggests its excellent rate capability. The capacitive performance of the $NiMoO_4$ electrode was evaluated using galvanostatic charge-discharge tests. Figure 4 (b) shows the charge-discharge curves of the electrode at different current densities. The nonlinear nature of the charge and discharge curves confirms the pseudo-capacitance behavior of the electrode [39], which is consistent with the CV results. The specific capacitance of the electrode is calculated using the following equation [39]:

$$Cs = I\Delta t / m\Delta V \quad \ldots. (1)$$

Where I is the discharge current, Δt is the discharge time, ΔV is the voltage window, and m is the mass of the active material. The calculated specific capacitance at 1 A g^{-1} is approximately 1180 F g^{-1} which is significantly higher than that of nanorods (367 F g^{-1}), nanotubes (864 F g^{-1}), nanoclusters (680 F g^{-1}) and hierarchical nanospheres (974 F g^{-1}) [1,27,30,33]. Figure 4 (c) shows the calculated specific capacitance as a function of current density. Table 1 summarizes the obtained specific capacitance of various $NiMoO_4$ electrodes with different morphologies. Note that most of the $NiMoO_4$ electrodes were fabricated on Ni foam substrates.

Figure 4 (d) shows the Nyquist plot of the sample in a frequency range of 0.2 Hz to 10 KHz. The observed semicircle in the high-frequency region is a result of the charge transfer

resistance (R_{ct}) that is associated with the redox reaction at the electrode's surface, and the straight line in the low-frequency region is attributed to the Warburg impedance (W_0), which measures the diffusion of the electrolyte within the electrode. The inset shows the corresponding equivalent circuit diagram where R_S represents the solution resistance and CPE is a constant phase element. The low charge transfer resistance of 0.49 Ω and Warburg impedance of 0.125 Ω is obtained from modeling (solid line), and these low R_{ct} and W_0 values contribute to the superior electrochemical performance of the electrode.

The electrochemical active surface area (ECSA) available for the electrochemical process can be estimated from the scan rate dependent CV characteristics in the non-faradaic region [40, 41]. Figure 5 (a) shows the CV curves of the $NiMoO_4$ electrode in the non-faradaic region. The ECSA is estimated using the following formula:

$$\text{ECSA} = C_{DL} / C_S \quad \ldots\ldots\ldots\ldots\ldots\ldots\ldots\ldots\ldots\ldots (2)$$

Where C_S is the specific capacitance for the electrolyte, and C_{DL} is the double-layer region specific capacitance. C_S = 0.040 $mFcm^{-2}$ for the KOH electrolyte [39]. The capacitive current (i_{DL}) in the non-faradic region is described by charge accumulation rather than redox reaction and can be expressed as follows:

$$i_{DL} = C_{DL} \cdot \times \nu \ldots\ldots\ldots\ldots\ldots\ldots\ldots\ldots\ldots\ldots\ldots\ldots (3)$$

Where ν represents the scan rate. Figure 5 (b) shows the capacitive current i_{DL} as a function of ν for the electrodes. The C_{DL} has directly obtained from the slope of the $i_{DL}(\nu)$ curves. The estimated ECSA value is 108.3 cm^{-2}. We use a Cs of 0.040 $mFcm^{-2}$ for the KOH electrolyte [39]. The observed ECSA values are very much higher than those of the reported values of other metal oxides [41].

The long-term cycling performance of the $NiMoO_4$ electrode is investigated for over 1000 cycles at a very high current density of 10 Ag^{-1}. Figure 6 (a) shows the specific

capacitance as a function of cycles. The specific capacitance decreases gradually with an increasing number of cycles. The capacity retention of the electrode after 1000 charge-discharge cycles is 27%. The specific capacitance loss during the cycling process is presumably due to structural damage at a very high current density [42, 43]. Compared with the retention data of other nanostructured nanospheres, for nanorods of NiMoO4 electrodes that are grown on Ni foam and carbon cloth [1, 4, 30] the obtained retention performance is less. The inferior retention performance of the $NiMoO_4$ nanoflake electrode grown on stainless steel is presumably because of the weak surface energy and adhesion which hinders the electrochemical properties.

The Ragone plot that relates the energy density (*E*) and power density (*P*) can be obtained from the GCD measurements using the following equations:

$$\mathrm{E} = \frac{1}{2} C_s (\Delta V)^2 \quad \ldots\ldots (4)$$

$$\mathrm{p} = \frac{E}{\Delta t} \quad \ldots\ldots (5)$$

Figure 6 (b) shows the Ragone plot of the $NiMoO_4$ electrode. The observed energy and power densities are superior to those of previously reported Ni-Mo based oxide electrodes [4] [7] [26].

4. Conclusions

A $NiMoO_4$ nano-flake thin film was successfully synthesized using the SILAR technique for supercapacitor electrode applications. The nanoflake thin film has a high electrochemical surface area, enhanced ion diffusion, and excellent electrical conductivity,

which results in superior electrochemical supercapacitor performance. The synergetic effect of nanoflake morphology and high electrochemical surface area created a specific capacitance of 1180 Fg^{-1} at a current density of $1Ag^{-1}$. The long-term electrochemical stability at a very high rate of 10 Ag^{-1} was obtained at which the sample maintained a capacitance of 600 Fg^{-1}. The sample had a specific energy density of 119 Wh/kg and a specific power density of 15709 w/kg. In future studies, the simple and profitable SILAR technique should be extended to other metal oxide systems to obtain promising electrochemical performance for energy storage applications.

Acknowledgments

The authors would like to thank the financial support from the National Research Foundation (NRF) of Korea (Grant nos. 2015M2A2A6A02045251, 2015R1D1A1A01060743, 2015R1A2A2A01004782, 2015R1D1A1A01058851 and 2015R1A2A1A15054906).

References

[1] D. Cai, D. Wang, B. Liu, Y. Wang, Y. Liu, L. Wang, H. Li, H. Huang, Q. Li, T. Wang, *ACS Appl. Mater. Interfaces* 2013, **5**, 2905−12910.

[2] J. R. Miller, P. Simon, *Science*. 2008, **321**, 651-652.

[3] P. Simon, Y. Gogotsi, *Nat. Mater*.2008, **7** , 845-854.

[4] S. Peng, L. Li, H. Bin Wu, S. Madhavi, and X. Wen Lou, *Adv. Energy mater*. 2015, **5**, 1401172.

[5] M.-C. Liu, L.-B. Kong, C. Lu, X.-J. Ma, X.-M. Li, Y.-C. Luo, L. Kang *J. Mater. Chem. A*. 2013, **1**, 1380-1387.

[6] B. Wang, S. Li, X. Wu, W. Tian, J. Liu and M. Yu. *J. Mater. Chem. A*. 2015, **3**, 13691-13698.

[7] K. Xiao, L. Xia, G. Liu, S. Wang, Liang-Xin Ding and H. Wang, *J. Mater. Chem. A*. 2015, **3**, 6128-6135.

[8] M. H. Yu, W. Wang, C. Li, T. Zhai, X. H. Lu and Y. X. Tong, *NPG Asia Mater*. 2014, **6**, 129.

[9] S. H. Choi, Y. N. Ko, J. K. Lee and Y. C. Kang, *Sci. Rep*. 2014, **4** , 5786.

[10] D. D. Li, L. X. Ding, S. Q. Wang, D. D. Cai, H. H. Wang, *J. Mater. Chem. A*. 2014, **2**, 5625.

[11] L. Zhan, S. Q. Wang, L. X. Ding, Z. Li and H. H. Wang, *Electrochim Acta*. 2014, **135**, 35.

[12] Z. Y. Wang, L. Zhou and X. W. Lou, *Adv. Mater*.2012, **14**, 1903.

[13] M. H. Chen, J. L. Liu, D. L. Chao, J. Wang, J. H. Yin, J. Y. Lin, H. J. Fan and Z. X. Shen, *Nano Energy*. 2014, **9**, 364.

[14] X. H. Lu, Y. X. Zeng, M. H. Yu, T. Zhai, C. L. Liang, S. L. Xie, M. S. Balogun and Y. X. Tong, *Adv. Mater*. 2014, **26**, 3148.

[15] H. G. Wang, D. L. Ma, Y. Huang and X. B. Zhang, *Chem.–Eur. J*. 2012, **18**, 8987.

[16] X. Yu, B. Lu, Z. Xu, *Adv. Mater*. 2014, **26**, 1044–1051.

[17] L. Q. Mai,F. Yang, Y. L. Zhao, X. Xu, L. Xu, Y. Z. Luo, *Nat. Commun*. 2011, **2**, 381.

[18] D. Ghosh, S. Giri, M. Moniruzzaman, T. Basu, M. Mandal, C. K. Das, *Dalton Trans*. 2014, **43**, 11067–11076.

[19] B. S. kumar, R. K. Selvan, *J. Colloid Interface Sci*. 2014, **426**, 280–286.

[20] L. Q. Mai, F. Yang, Y. L. Zhao, X. Xu, L. Xu and Y. Z. Luo, *Nat. Commun*. 2011, **2**, 381.

[21] X. Z. Yu, B. G. Lu and Z. Xu, *Adv. Mater*. 2014, **26**, 1044.

[22] D. P. Cai, B. Liu, D. D. Wang, L. L. Wang, Y. Liu, H. Li, Y. R. Wang, Q. H. Li and T. H. Wang, *J. Mater. Chem. A*. 2014, **2**, 4954.

[23] P. R. Jothi, K. Shanthi, R. R. Salunkhe, M. Pramanik, V. Malgras, S. M. Alshehri, and Y. Y. Eur. *J. Inorg. Chem*. 2015, 3694–3699.

[24] J. Haetge, I. Djerdj and T. Brezesinski, *Chem. Commun*.2012, **48**, 6726.

[25] W. Xiao, J. S. Chen, C. M. Li, R. Xu and X. W. Lou, *Chem. Mater*.2010, **22**, 746.

[26] D. Guo, Y. Luo, X. Yu, Q. Lin, T. Wangnn, *Nano Energy*.2014, **8**, 174–182.

[27] H. Wan, J. Jiangn, X. Ji, L. Miao, L. hang, K. Xu, H. Chen, Y. Ruan, *Materials Letters*.2013, **108**,164–167.

[28] D. Cai, B. Liu, D. Wang, Y. Liu, L. Wang, Han Li, Y. Wang,. C. Wang, Q. Li, T. Wang , *Electrochimica Acta*. 2014, **115**, 358– 363.

[29] D. Cai, B. Liu, D. Wang, Y. Liu, L. Wang, Han Li, Y. Wang, C. Wang, Q. Li, T. Wang, *Electrochimica Acta*. 2014, **125**, 294–301.

[30] D. Ghosh, S. Giri and C. K. Das, *Nanoscale*.2013, **5**, 10428.

[31] B. Wang, S. Li, X. Wu, J. Liu and W. Tian, *Chem. Phys*.2016, **18**, 908-915.

[32] D. Guo, P. Zhang, H. Zhang, X. Yu, J. Zhu, Q. Li, T. Wang, *J. Mater. Chem. A*, 2013, **1**,9024.

[33] Z. Yin, S. Zhang, Y. Chen, P. Gao, C. Zhu, P. Yang, L. Qia, *J. Mater. Chem. A*, 2015, **3**, 739.

[34] L. Huang, J. Xiang, W. Zhang, C. Chen, H. Xu, Y. Huang, *J. Mater. Chem. A*, 2015, **3**, 22081.

[35] a) H. M. A. Dayem, *Ind. Eng. Chem. Res*. 2007, **46**, 2466–2472;

b) A. Maione, M. Devillers, *J. Solid State Chem*.2004, **177**, 2339–2349.

[36] Israel E. Wachs, Charles A. *Roberts Chem. Soc. Rev*.2010, **39**, 5002–5017.

[37] A. I. Inamdar, R. S. Kalubarme, J. Kim, Y. Jo, H. Woo, S. Cho, S. M. Pawar, Chan-Jin Park, Young-Woo Lee, J. I. Sohn, S. Cha, J. Kwak, H. Kim, H. Im, *J. Mater. Chem. A*, 2016, **4**, 4691.

[38] D.L. Li, Y.N. Gong, Y.P. Zhang, C.Z. Luo, W.P. Li, Q. Fu, C. X. Pan, *RSC Adv*. 2016, **6**, 1380-1387.

[39] A.I. Inamdar , Y. Kim, S.M. Pawar, J.H. Kim, H. Im, H. Kim, *Journal of Power Sources*.2011, **196**, 2393–2397.

[40] V. Kannan, A.I. Inamdar, S.M. Pawar, H.S. Kim, H.C. Park, H. Kim, H. Im, and Y.S. Chae, *ACS Appl. Mater. Interfaces*. 2016, **8**, 17220−17225.

[41] McCrory, C. C. L. Jung, S.; Peters, J. C.; Jaramillo, *J. Am. Chem. Soc*. 2013, **135**, 16977−16987.

[42] Liu, M. C., Kong, L. B.,Lu, C., Ma, X. J., Li, X. M., Luo, Y. C., Kang, L. *J. Mater. Chem. A*. 2013, **1**, 1380−1387.

[43] J.Y. Lei, Z.Q. Jiang, X.F. Lu, G.D. Nie, C. Wang, *Electrochim Acta*. 2015, **176**, 149-155.

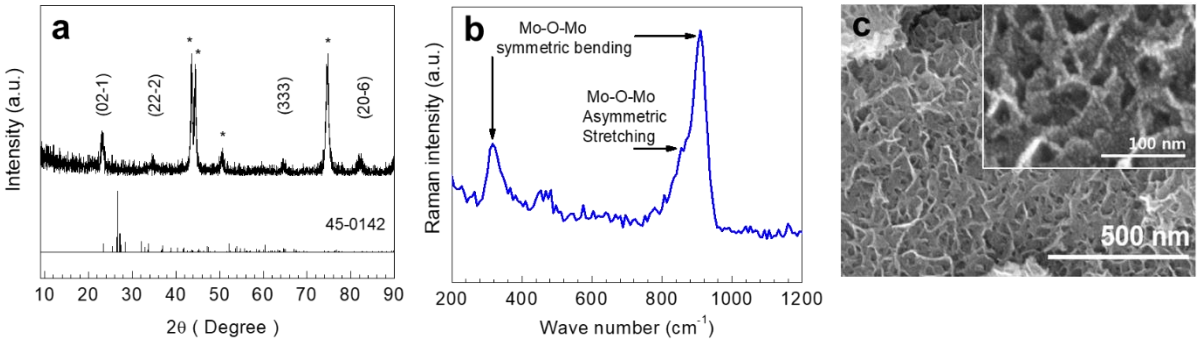

Figure 1. (a) X-ray diffraction patterns of $NiNoO_4$ along with standard JCPDS (45-0142) data. The star symbol (*) indicates the substrate peaks, (b) Raman spectra of the $NiMoO_4$ thin film measured in the range of 200-1200 cm^{-1}, suggesting the formation of $NiMoO_4$, (c) Scanning electron micrographs of $NiMoO_4$ thin film showing a house-of-cards-like nano-flex morphology.

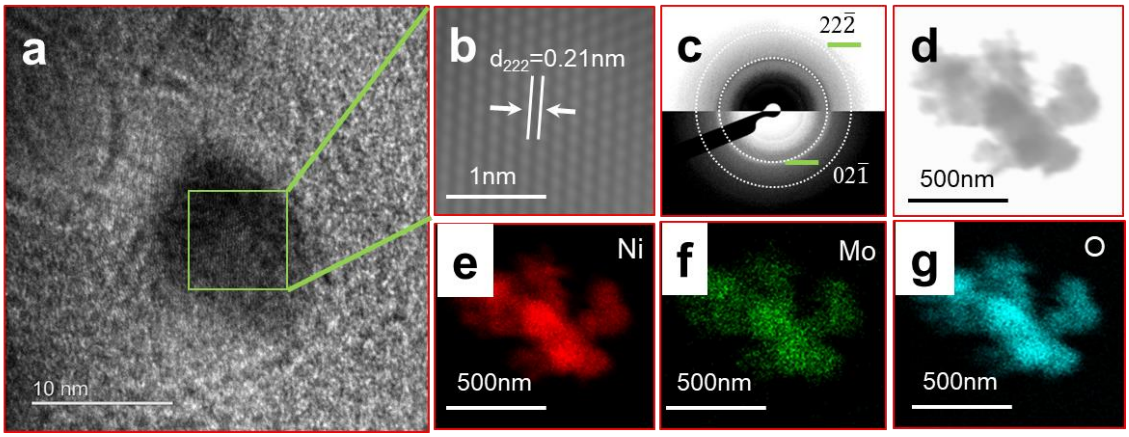

Figure 2. (a, b) High-resolution TEM, (c) selective area electron diffraction (SAED), (d-g)

elemental mapping results from the STEM characterizing of $NiMoO_4$.

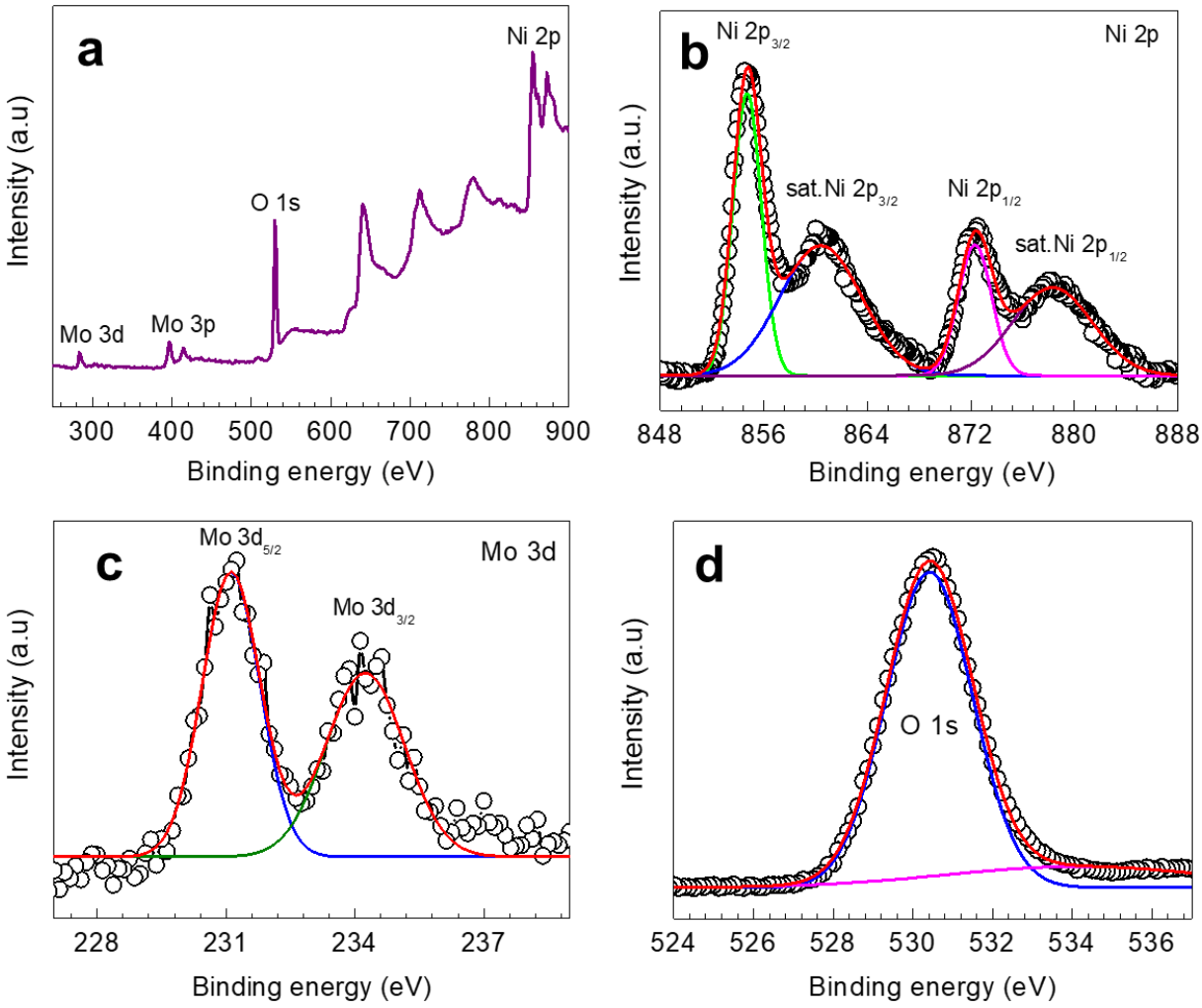

Figure 3. X-ray photoelectron spectroscopic data of $NiMoO_4$ thin film. (a) Survey spectra revealing the existence of Ni, Mo, and O as constituting elements. Core-level X-ray photoelectron spectra for (b) Ni 2p, (c) Mo 3d, and (d) O 1s.

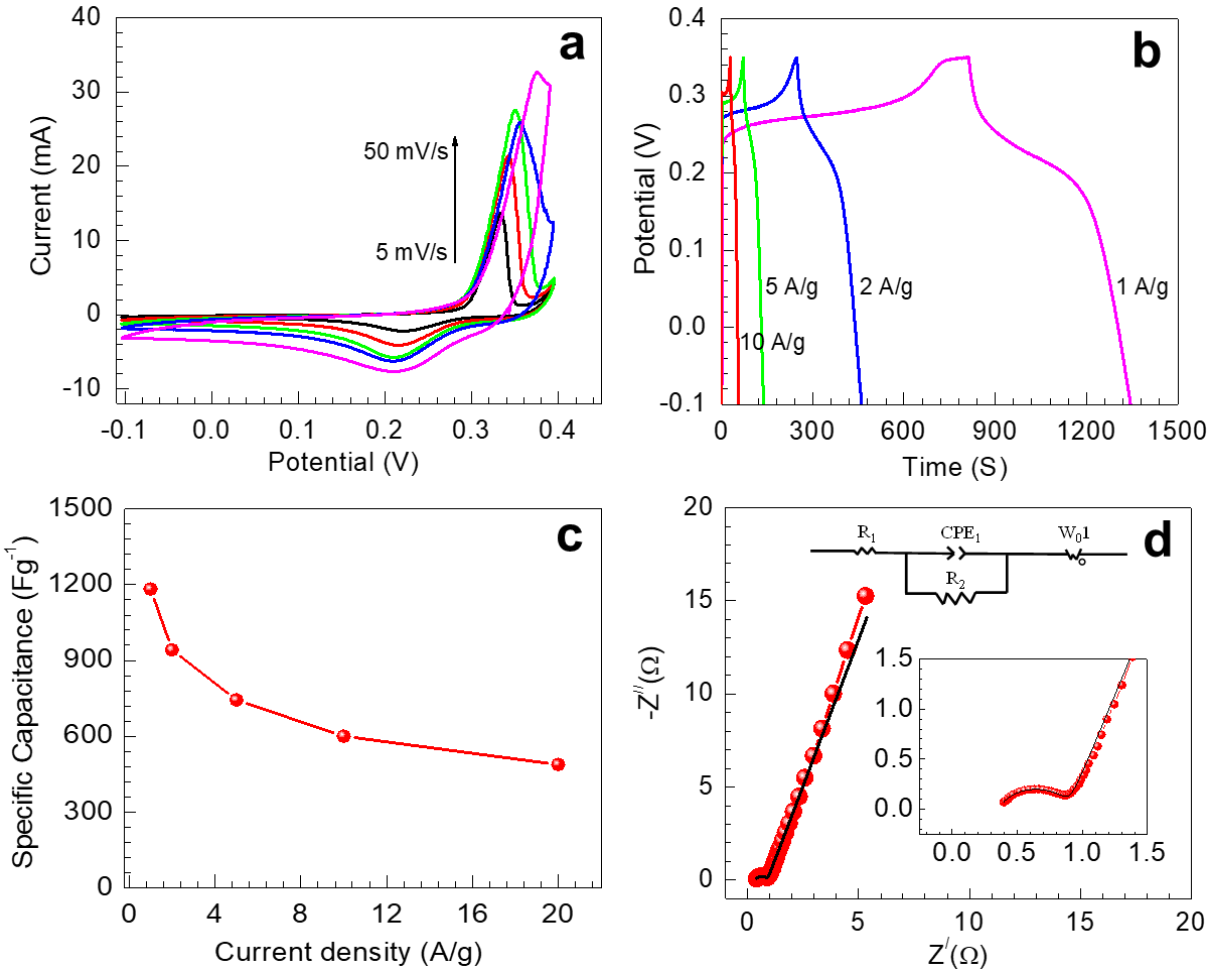

Figure 4. (a) CV curves of $NiMoO_4$ thin film measured at different scan rates: 10, 20, 30, 50, 100 mV/s, (b) galvanostatic charge-discharge curves of $NiMoO_4$ thin film at 1, 2, 5, 10, 20 Ag^{-1}, (c) specific capacitance obtained for $NiMoO_4$ thin film as a function of current density, (d) Nyquist plots of $NiMoO_4$ thin film, measured in the frequency range of 0.2 Hz to 10 KHz. The inset shows the equivalent circuit diagram.

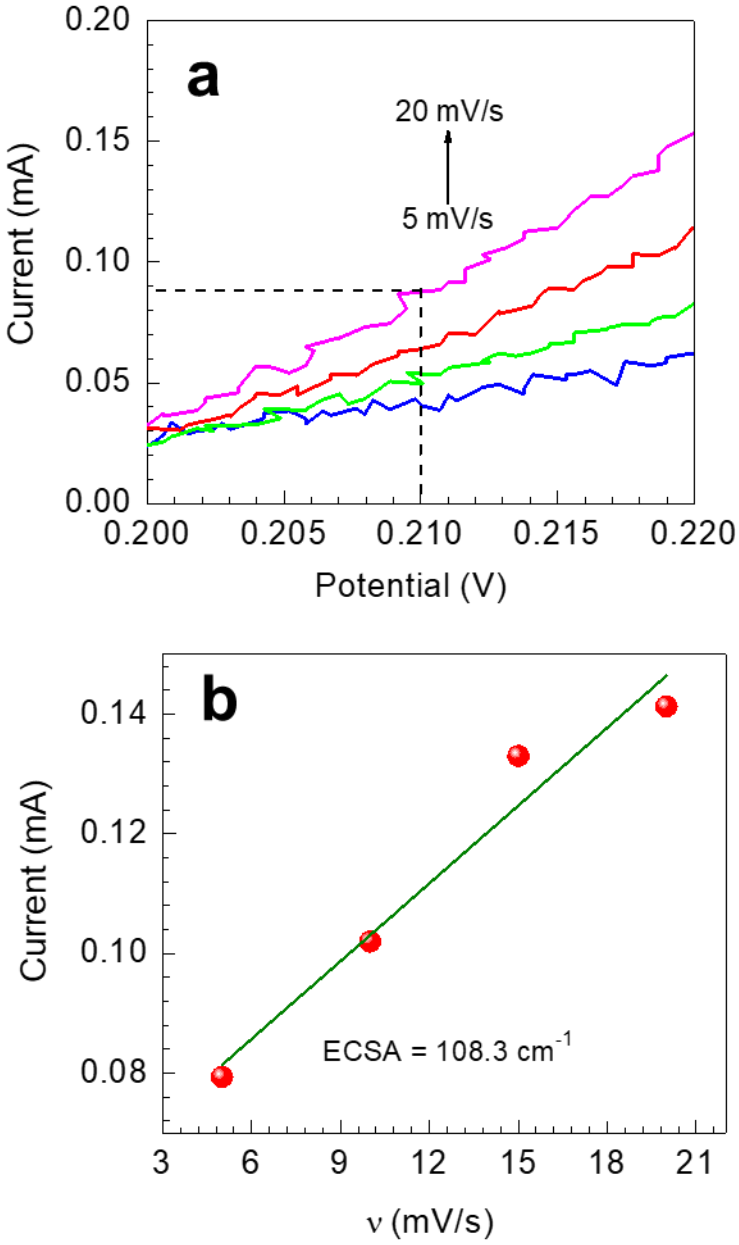

Figure 5. (a) CV curve of $NiMoO_4$ thin film in the linear non-faradaic charging region at different scan rates from 5 to 20 mV/s and (b) non-faradaic current density obtained from the CV curves at 0.21 V as a function of scan rate (ν).

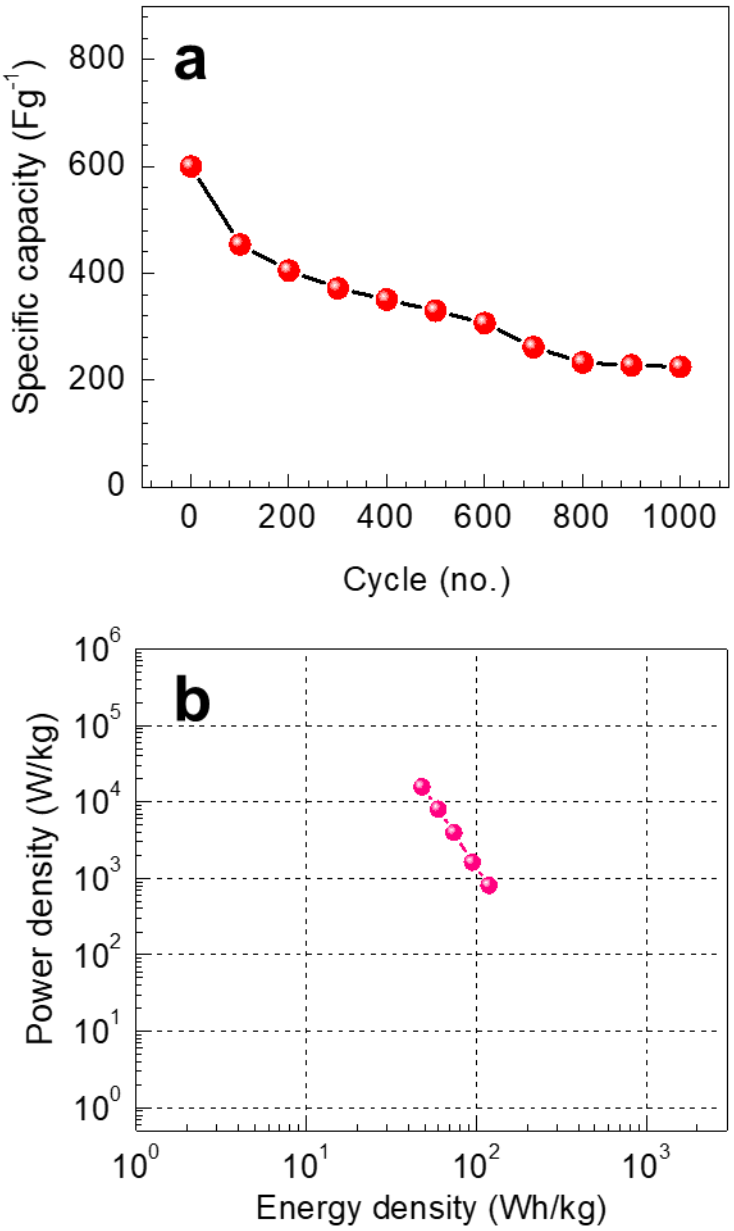

Figure 6. (a) Specific capacitance of $NiMoO_4$ thin film measurements at a high current density of 10 Ag^{-1} during 1000 charge/discharge cycles, and its retention, (b) Ragone plot showing the relation of energy density and power density.

Table 1. Electrochemical Supercapacitor properties of various $NiMoO_4$ morphologies reported in the literature.

Material and Morphology	**Substrate**	**Capacity ($1Ag^{-1}$)**	**Method**	**Electrolyte**	**Ref. No**
$NiMoO_4$ Nano-flake	Stainless steel	1180 Fg^{-1}	SILAR	2 M KOH	This work
$NiMoO_4$Nano-rods and HierarchicalNano-spheres	Ni foam	974 Fg^{-1}	Hydrothermal	3 M KOH	1
$NiMoO_4$ Nano-rod and nano-sheet	Ni foam	1221.2 vs 1091.1 Fg^{-1}	Hydrothermal	2 M KOH	4
Network-like porous $NiMoO_4$	Ni foam	1155.54 mAh g^{-1}	CVD/hydrothermal	1 M LiPF6	6
Honeycomb-like $NiMoO_4$	Ni foam	1694 Fg^{-1}	Hydrothermal	1 M KOH	7
$NiMoO_4$ nanowires	carbon cloth	1587 Fg^{-1}	Hydrothermal	2 MKOH	26
$NiMoO_4xH_2O$ nanoclusters	Ni foam	680 Fg^{-1}	Facile and rapid microwave-assistedmethod	6 MKOH	27
$NiMoO_4$ nano-sheets	carbon black	1654 Fg^{-1}	Hydrothermal	3 M KOH	28
$NiMoO_4$ nano-sheets	Ni foam	3205 Fg^{-1}	Hydrothermal	1.5 M LiOH	29
$NiMoO_4$$nH_2O$ nano-rods†	Ni Foam	367 Fg^{-1}	Hydrothermal		30
Hierarchical $NiMoO_4$ nano-wire	Ni foam	1088.02 mAh g^{-1}	CVD	1 M LiPF6	31
$NiMoO_4$ nano-wires	Ni foam	1308 Fg^{-1}	Hydrothermal	2 M KOH	32
Nano-sheet based $NiMoO_4$ nano-tubes	Ni foam	864 Fg^{-1}	Hydrothermal		33
$NiMoO_4$ nano-plate	Ni foam	2138 Fg^{-1}	Hydrothermal	$3moll^{-1}$ 1KOH	34